Vectorial mechanism of nonlinearity enhancement in rubidium vapor

Nikolai Korneev* and Chrystian Gutiérrez Parra

Instituto Nacional de Astrofísica, Óptica y Electrónica, Av. Luis Enrique Erro No. 1, Sta. Ma. Tonantzintla, Puebla 72840, Mexico
**Corresponding author: korneev@inaoep.mx*

Received May 18, 2012; revised July 21, 2012; accepted July 27, 2012;
posted July 27, 2012 (Doc. ID 168767); published August 31, 2012

We report the calculations of vectorial nonlinear properties of rubidium vapor for ^{87}Rb D_2 transition at moderate intensities. The results are compared with self-rotation and diffraction experiments. Different from Kerr nonlinearity, optimal intensity exists here, which depends on beam geometry. For intensities close to the optimal, the vectorial mechanism is much more efficient than a scalar one, and strong self-action for wide beams can be obtained with it.

OCIS codes: 190.2055, 190.4223, 190.5940.

1. INTRODUCTION

Rubidium vapor for laser frequency, close to the transition frequency, is well known as nonlinear optical medium [1]. Strong self-action effects, including pattern formation, were observed in it with high power focused beams. For theoretical description, the nonlinearity is usually taken in a simple scalar Kerr form [2]. For laser frequency far enough from the transition, the Kerr coefficient can be obtained from the two-level model as a result of saturation; the nonlinear addition to refractive index is proportional to light intensity I and inversely proportional to the detuning cube Δ^3 [1]:

$$n_2 \sim I/\Delta^3. \tag{1}$$

For multilevel atoms and strong laser fields, however, the effects of atomic coherence can become important. In this case the level populations alone are not sufficient to explain the medium response to light, and it is necessary to consider phase information of atomic state or a density matrix. The coherent effects actively studied actually include among others electromagnetically induced transparency [3], dark states [4], and nonlinear magneto—optical effects [5]. Polarized light is important in creating atomic coherence, and thus nonlinearities can be strongly modified (enhanced or diminished) by manipulations with light polarization. Complicated vectorial nonlinear effects are observed in rubidium as well. Particularly, applications such as ultralow energy optical switching [6], squeezed vacuum generation [7–9], precise magnetometry [10,5], slow light [11], Doppler spectroscopy [12], and nonlinear resonances [13] are related to the nonlinear modification of the polarization state of light. There are analytic solutions for saturated absorption spectra using rate equations of the rubidium [14]. Though general mechanisms are quite well understood, an adequate theoretical description for experimentally important intensities and detunings is difficult because of the multilevel structure of rubidium transition.

We present results of nonlinearity calculation, based on the direct solution for density matrix evolution in the ^{87}Rb D_2 line. The solution procedure is similar to the one reported in [15,16]. The model, though it is numerically intensive, does not have fitting parameters and the results are in good qualitative agreement with experimentally observed nonlinearity behaviour. The results show that the vectorial interaction for intensities typical of tunable semiconductor lasers do not demonstrate a simple Kerr character suggested by Eq. (1). Instead, there is an optimal light intensity, for which the nonlinearity is the highest, and this optimal intensity depends on time of flight (beam diameter). The nonlinearity has nontrivial spectral dependences as well.

For moderate light intensities in the 10 mW/mm^2 range, the optimal cross-phase modulation (manifested in three-wave mixing experiments) can be much more effective than the standard Kerr self-phase mechanism. Further nonlinearity enhancement can be obtained by using elliptic polarization combined with weak longitudinal magnetic field. We perform experiments, which confirm the general validity of the theoretical description. Since the nonlinearity can be positive in a part of the Doppler-broadened line, it is possible to obtain an exponential amplification of weak signal beams through modulation instability mechanism, using appropriate parameters such as beam geometry, intensity, and polarization. This process, in ^{87}Rb $Fg = 2$ transition for beam intensities in 10 mW/mm^2 range, gives net gains in excess of 100 and relative gains (taking into account absorption) in excess of 1000; thus it can lead to strong beam profile modification upon propagation, which is also demonstrated.

2. THEORETICAL MODEL

We work with a basis of circular polarization amplitudes σ_1, σ_2, and we use the equivalent Rabi frequencies Ω_1, Ω_2. The two components of nonlinear medium polarization can be written, when we take the account into the rotational symmetry of problem, for longitudinal magnetic field in the form ($i = 1, 2$)

$$P_i = F_i(|\sigma_1|, |\sigma_2|)\sigma_i = F_i(\Omega_1, \Omega_2)\sigma_i. \quad (2)$$

For experimentally important intensity levels, the medium polarization is not meaningfully represented as a series in powers of amplitudes. The physical situation that we consider is an interaction of a strong pump beam with a weak probe. The probe slightly changes the pump intensity and/or polarization state, and the additions are assumed to be small. The nonlinear interaction in a number of practically interesting cases is given by a 2 by 2 matrix, estimated for the pump parameters and proportional to

$$\begin{matrix} \frac{\partial F_1}{\partial \Omega_1}\Omega_1 & \frac{\partial F_1}{\partial \Omega_2}\Omega_2 \\ \frac{\partial F_2}{\partial \Omega_1}\Omega_1 & \frac{\partial F_2}{\partial \Omega_2}\Omega_2 \end{matrix}. \quad (3)$$

Such a matrix appears when we consider the first approximation of the three-wave mixing, including the strong pump and a pair of weak symmetric side orders. The matrix eigenvectors give the proper polarizations of side beams, which are maintained along propagation, and corresponding eigenvalues give equivalent Kerr constants for a polarization in question. Mathematically, the problem for proper polarization is then reduced to a scalar Kerr interaction, which gives a well-known modulation instability type solution for positive eigenvalues.

Solving the eigenvalue problem for the matrix Eq. (3) is trivial once the medium polarization in the function of Rabi frequencies is known. In particular, for linear polarization of a pump ($\Omega_1 = \Omega_2$) and zero magnetic field, the matrix is symmetric, and there are two proper polarizations of probe beam, corresponding to parallel to pump ($\sigma_{s,1} = \sigma_{s,2}$) and orthogonal to pump ($\sigma_{s,1} = -\sigma_{s,2}$) linear polarization. Their eigenvalues are

$$\eta_\pm = \frac{\partial F_1}{\partial \Omega_1}\Omega_1 \pm \frac{\partial F_1}{\partial \Omega_2}\Omega_2, \quad \text{for } \Omega_1 = \Omega_2 = \Omega. \quad (4)$$

The η_+ coefficient describes the self-phase modulation, and it gives the usual scalar Kerr nonlinearity. The η_- coefficient determines an interaction of a linearly polarized pump beam with orthogonally polarized signal beam. We also note that η_- gives the difference of refractive index for two circular components in response to the polarization ellipticity, i.e., this coefficient describes the amount of polarization self-rotation. Thus, η_- is easily determined in the experiment directly. The ellipticity coefficient ε is determined as follows [17]:

$$\tan \varepsilon = \frac{\sigma_2 - \sigma_1}{\sigma_2 + \sigma_1}. \quad (5)$$

Following [18], to calculate medium polarizations we use the master equation for density matrix ρ evolution:

$$\frac{\partial \rho}{\partial t} = (i/\hbar)[\rho, H] + \sum_{q=-1,0,1} C_q \rho C_q^+ - \frac{1}{2}(C_q^+ C_q \rho + \rho C_q^+ C_q), \quad (6)$$

where H is the Hamiltonian of an atom, and C_q, C_q^+ are lowering and raising atomic operators:

$$\begin{aligned} C_q^+ |F_g, m_{F_g}\rangle &= \Gamma^{1/2}(1, F_g, q, m_{F_g}; F_e, m_{F_e} = m_{F_g} + q)|F_e, \\ & m_{F_e} = m_{F_g} + q\rangle, \\ C_q^+ |F_e, m_{F_e}\rangle &= 0, \\ C_q &= (C_q^+)^*, \end{aligned} \quad (7)$$

with a decay rate Γ, and Clebsch-Gordan coefficients for coupling ground and excited states sublevels [19].

The evolution given by the Eq. (6) is calculated numerically for a characteristic time of flight τ, using a fast special algorithm described in [15,16]. The derivatives in Eq. (3) are calculated numerically using close values of Rabi frequencies for a necessary number of detunings (typically around 100). After this, the convolution with Doppler lineshape is performed, which gives the approximation to experimentally observable spectra. Different from other calculations with full level structure of ^{87}Rb D_2 line reported in literature, we do not assume equivalent steady state with some effective level pumping, and we solve for complete time evolution. Thus, our calculation has no fitting parameters but requires much more computational effort.

3. RESULTS OF NUMERICAL MODELLING

We first concentrate on the case of zero magnetic field and linear pump polarization in $F_g = 2$ ^{87}Rb D_2 line (780.24 nm). The interest in this particular transition is due to two reasons. First, in this line the highest three-wave mixing gain is observed for intensities in 10–30 mW range of laser power, and second, calculations in ^{87}Rb are somewhat faster than in ^{85}Rb because of smaller sublevel number for this isotope. For this numeric model we considered a temperature of 300 °K, (density of the vapor 1×10^{13} cm^{-3}) and the Doppler broadened linewidth about 500 Mhz.

The spectra of cross-phase modulation coefficient η_- prove to be strongly dependent on the time of flight and light intensity (Figs. 1 and 2). The character of the curve changes in a nontrivial way. The parameter, which describes the shape of the curve, is approximately the "exposition" $W = I\tau$. In particular, the curve giving the biggest η_- for a given time of flight is well described by the condition $W = \text{const}$. However, smaller intensities and bigger flight times (wider beams) give somewhat higher maximal nonlinearity values in a positive spike (Fig. 1). For a negative spike the difference is small. The action of making intensity higher with a fixed time of flight is similar to making bigger the time of flight with a fixed intensity (Fig. 2). With fixed beam diameter, there are two optimal light intensities that are close to 2 mW/mm^2 and 34 mW/mm^2. The smaller characteristic intensity gives positive nonlinearity at the red-shifted wing of the line. For beams of ~1 mm diameter, the optimal intensity has an order of 1–10 mW/mm^2. By raising this intensity approximately one order of magnitude, the positive spike is eliminated, and the negative one appears at the opposite wing of the line. Raising intensity above the second optimal value gives diminished nonlinearity (Fig. 2) and extends the spectrum to the high-frequency region.

Thus, the cross-phase modulation inside the absorption line manifests itself as a substantially transient effect, which has complicated dependence on the time of flight.

The nonlinearity can be further enhanced with a combination of a weak magnetic field and elliptic polarization of a

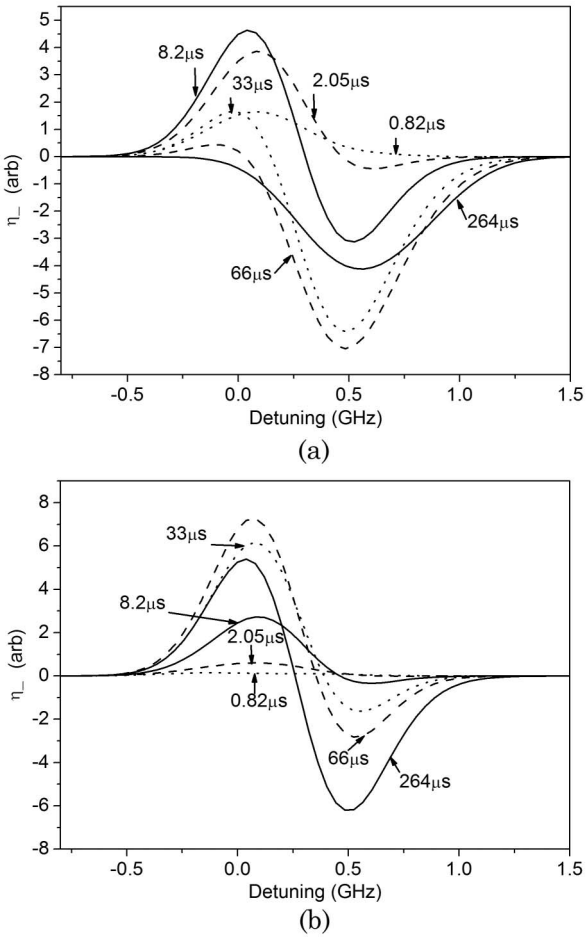

Fig. 1. Cross-phase modulation spectra in $F_g = 2$ line for two intensities (a) 8.54 mW/mm^2 and (b) 0.53 mW/mm^2, both with different times of flight. The zero frequency corresponds to $F_g = 2$, $F_e = 2$ transition.

pump (either of these factors separately diminishes nonlinearity strength). For higher intensities, both the elliptic polarization and the magnetic field are necessary for a bigger maximal nonlinearity. For a low intensity (2.1 mW/mm^2) and linear polarization we observed that the positive peak of the cross-phase modulation spectra is reduced depending on

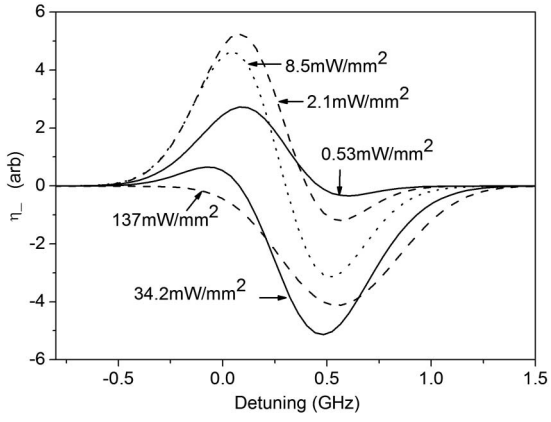

Fig. 2. Cross-phase modulation spectra in $F_g = 2$ line for time of flight 8.2 μs and different intensities.

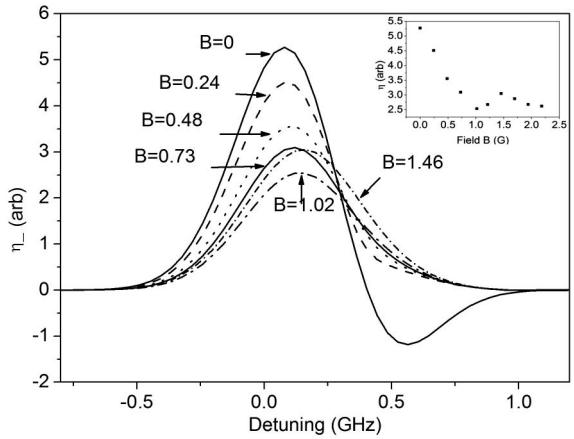

Fig. 3. Cross-phase modulation spectra for linear polarization, time of flight 8.2 μs, intensity 2.1 mW/mm^2, and different magnetic fields. The inset shows the maximum absolute value of each spectra in function of magnetic field.

the magnetic field applied (Fig. 3). The relative importance of different nonlinear processes near the lower optimum intensity is shown in Fig. 4. It is seen, that for moderate intensity one can expect approximately an order of magnitude nonlinearity strength growth if vectorial nonlinearity is used instead of a traditional Kerr one. Figures 5 and 6 show that the nonlinearity is increased when the magnetic field is applied, until it reaches a maximum, and it decreases for still higher fields. When we have a small ellipticity ($\varepsilon = -0.061$) it reaches a maximum with a small magnetic field ($B = 0.51$ G); for a greater ellipticity ($\varepsilon = -0.116$) we need a bigger magnetic field value ($B = 0.87$ G). For a given time of flight and intensity there is only one combination of ε and B which gives an optimal nonlinearity.

Note also that the signs of scalar and vectorial nonlinearity are generally opposite. This feature is quite useful from the experimental point of view if we are interested in weak beam amplification. It is possible to obtain positive nonlinearity at the red-shifted wing of ^{87}Rb, and this wing does not overlap with ^{85}Rb line. Thus, natural rubidium can be used instead of isotopically pure rubidium.

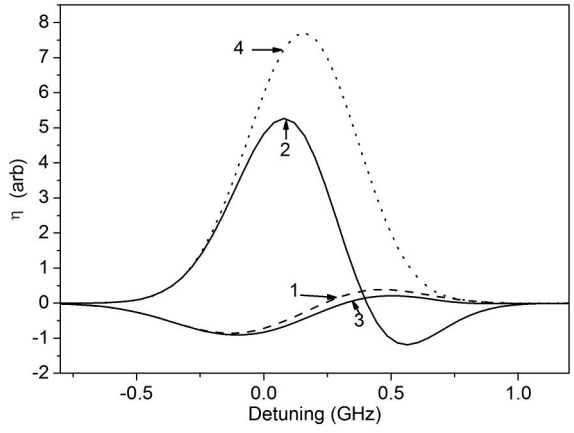

Fig. 4. Curve 1: zero magnetic field, η_+. Curve 2: zero magnetic field, η_- with ellipticity $\varepsilon = 0$. Curves 3 and 4: two eigenvalues for ellipticity $\varepsilon = -0.061$, and magnetic field $B = 0.51$ G. Time of flight 8.2 μs, intensity 2.1 mW/mm^2.

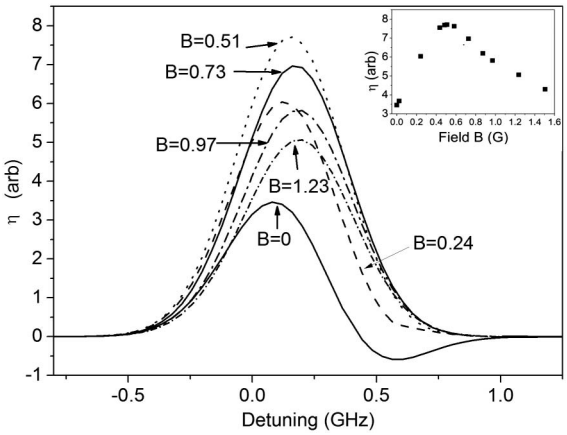

Fig. 5. Eigenvalues for ellipticity $\varepsilon = -0.061$ and different magnetic fields. Time of flight 8.2 μs, intensity 2.1 mW/mm^2. The inset shows the maximum absolute value of each eigenvalue in function of magnetic field.

In $F_g = 1$ transition, the qualitative behavior is quite similar to $F_g = 2$ line. Here, $W = I\tau$ better describes the curve shape, than for $F_g = 2$; thus we show only the intensity dependence with fixed time of flight (Fig. 7). We can see that the characteristic intensity, for which the cross-phase modulation is maximal, is approximately 10 times smaller than for $F_g = 2$, and the maximal value of nonlinearity is ~2.5–3 times lower. The advantage for cross-phase modulation and enhancement with elliptic polarization and magnetic field are observed as well, though the gain is smaller here (Figs. 8, 9). Experimentally, as well as in theory, for the same geometry, temperature, and corresponding optimal intensities, the diffraction efficiency obtained in $F_g = 2$ is higher; thus we concentrate mainly on this line. However, for high diffraction efficiency in $F_g = 2$ with beams of ~1 mm diameter, laser powers 10–20 mW are needed, and for $F_g = 1$, 1–2 mW it is sufficient.

Note also that to enhance the nonlinearity in $F_g = 1$ transition we need a magnetic field with an opposite sign with respect to that one for $F_g = 2$ transition (Fig. 8).

The theoretical results are obtained for constant light intensity and polarization. They suggest that the nonlinearity of interest depends on the whole history of atom illumination, thus

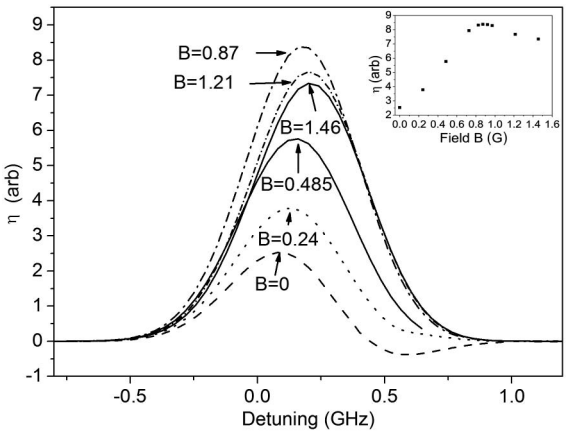

Fig. 6. Eigenvalues for ellipticity $\varepsilon = -0.116$ and different magnetic fields. Time of flight 8.2 μs, intensity 2.1 mW/mm^2. The inset shows the maximum absolute value of each eigenvalue in function of magnetic field.

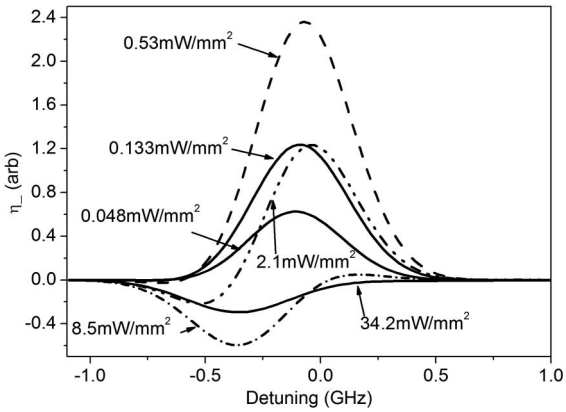

Fig. 7. $F_g = 1$ transition, cross-phase modulation spectra for time of flight 8.2 μs and different intensities.

the nonlinearity is strongly non-local. The calculation for the center of uniform cylindrical beam can be made exactly by averaging over the arrival times, but calculations for variable intensity beams (in particular, for Gaussian beams and/or interference fringes) will result in further order of magnitude increase of calculation times, which are already quite big. Thus, for comparison with experiment we limit ourselves to qualitative features that follow from the theory, and we do not try exact curve fitting.

4. EXPERIMENT

In our experiments, we used 75 mm long natural rubidium cell placed inside two protective shells made of μ-metal. The electric heater was placed between the two shells. Longitudinal magnetic field is produced with a solenoid. We were using 50 mW tunable external cavity diode laser.

First, we performed measurements of self-rotation with a simple setup described in [20]. The polarization state of incoming light was changed by a quarter-wave plate, rotated by ±6 degrees. The beam passed through the cell, and its two orthogonally polarized components were sent through polarizing beamsplitter to two photodiodes. The beamsplitter rotation angle was adjusted in order to have equal photodiode readings outside of absorption lines. The two photodiode

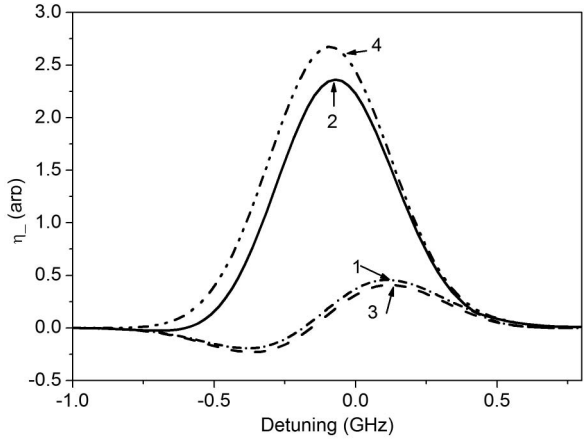

Fig. 8. $F_g = 1$ transition, curve 1: zero magnetic field, η_+. Curve 2: zero magnetic field, η_- with ellipticity $\varepsilon = 0$. Curves 3 and 4: two eigenvalues for ellipticity $\varepsilon = -0.119$, and magnetic field $B = -0.73$ G. Time of flight 8.2 μs, intensity 0.53 mW/mm^2.

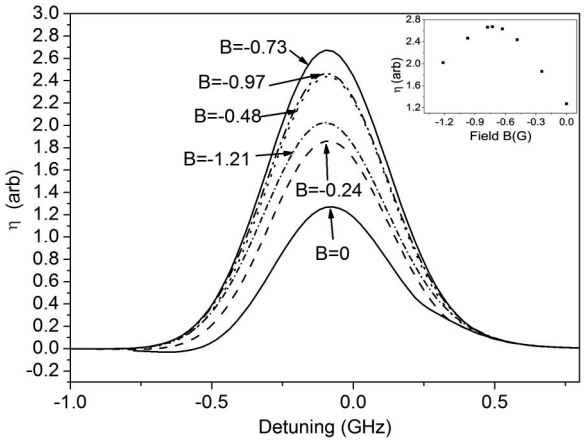

Fig. 9. $F_g = 1$ transition, eigenvalues for ellipticity $\varepsilon = -0.119$, and different magnetic fields. Time of flight 8.2 μs, intensity 0.53 mW/mm^2. The insert shows the maximum absolute value of each eigenvalue in function of magnetic field.

signals were digitally subtracted and filtered. Finally, the curves for +6 and −6 degrees (which have opposite signs) were subtracted again and divided by a photodetector reading outside the line. This magnitude is proportional to rotational angle in question [21]. In order to minimize the absorption influence, we performed measurements at room temperature ($T = 22\,^{\circ}$C). The results for two different beam diameters are presented in Figs. 10 and 11. The first beam was obtained by expanding the laser output with a telescopic system. The measured beam radius (called r) inside the cell (at $1/e$ intensity level) is $r = 0.82 \pm 0.02$ mm. The narrow features are due to the reflection from the back window of the cell, which is difficult to avoid for beams with a wide diameter. For narrow beam of Fig. 11, an inclination of a cell is sufficient to eliminate the influence of reflection.

The second set of curves was obtained by loosely focusing a beam with big focal length lens into a cell, which produced Gaussian beam radius of 0.17 ± 0.02 mm. In both cases a 0.5 mm diameter diaphragm was placed in a far field before the detecting beamsplitter to measure the rotation in a beam centre.

The behavior of these curves is generally consistent with a theoretical analysis in Figs. 1 and 2. In particular, the optimal

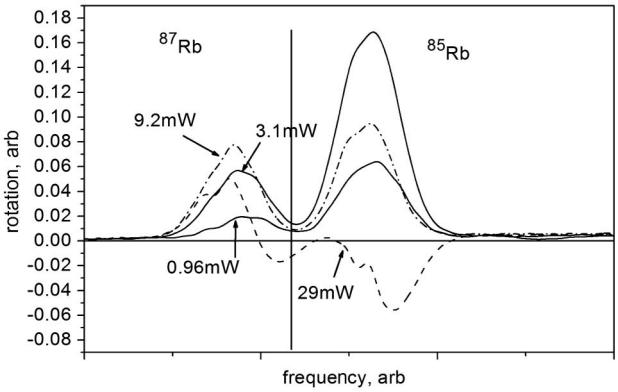

Fig. 10. Self-rotation signal for different beam powers. The Gaussian beam radius is $r = 0.82$ mm. The behavior in ^{87}Rb Fg = 2 transition (left spike) qualitatively corresponds to the theoretical curves in Fig. 2.

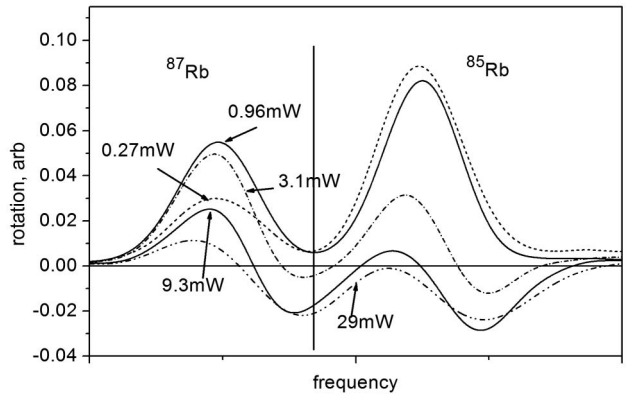

Fig. 11. Self-rotation signal for different beam powers. Similar to Fig. 10, but the Gaussian beam radius is $r = 0.17 \pm 0.02$ mm.

light intensity is clearly seen for both beam widths. For more narrow beams, the optimal intensity, proportional to P/r^2 (P is a beam power), is bigger than for a wider one, and the maximal obtainable rotation angle is somewhat smaller.

To compare the relative strengths of self-phase modulation and the cross-phase modulation process we have crossed a strong pump beam, $P = 19$ mW, $r = 0.58$ mm with a weak signal beam (0.6 mW) at a small angle of 7 mrad. The setup was similar to that one used in [15]. The cell was heated to 78 °C to obtain better diffraction efficiency, though for such temperatures the absorption is not small. As a result, diffraction in a conjugated order can be observed. To detect weak diffraction on the background of a strong pump beam wing we were chopping the signal beam with 0.5 kHz frequency and measuring the photodetector output in a conjugate order with a lock-in amplifier in function of laser frequency across the line. The signal beam polarization could be changed from parallel to orthogonal with a half-wave plate. Additional quarter-wave plate served to make both pump and signal elliptically polarized. Though the diffracted wave intensity is not directly proportional to the nonlinearity strength here, the relative importance of different processes is clearly seen in Fig. 12.

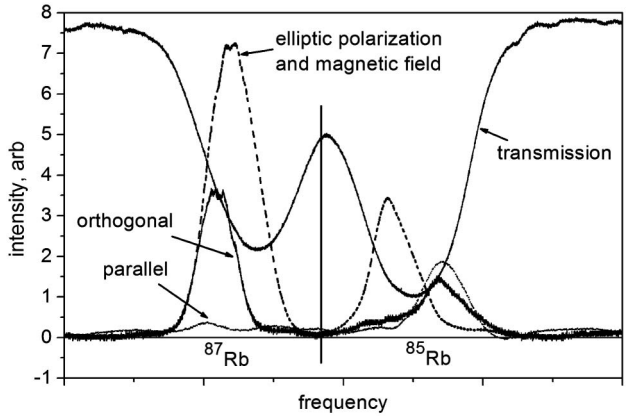

Fig. 12. Spectral dependences of pump beam transmission through the cell (fine line) and diffracted wave intensity for different combinations of signal and pump polarizations. We have two signals with polarizations parallel to pump and orthogonal to pump, respectively, both with linear polarization of pump and zero magnetic field. Dashed line is for a pump beam ellipticity ~0.07 and a magnetic field $B = 0.58$ G. The results in ^{87}Rb Fg = 2 transition (left spike) are related to the theoretical curves in Fig. 4.

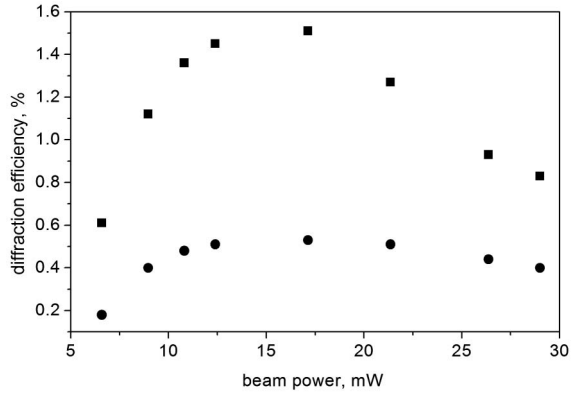

Fig. 13. Diffraction efficiency in a conjugated beam for $B = 0$, linear pump polarization, and cross-polarized signal beam in function of laser power. Circles: ratio of diffracted beam intensity to input pump beam intensity. Squares: ratio of diffracted beam intensity to output pump intensity. The difference is due to absorption, which is intensity dependent. All values are taken for the laser frequency giving maximal diffracted beam intensity.

For linearly polarized pump, the orthogonal polarization of signal gives much bigger diffracted signal than the parallel polarization. By making a pair polarization elliptical with a common quarter wave plate and applying a weak magnetic field, the diffraction strength can be further enhanced.

By comparing this to Fig. 4 we see that the theory adequately describes the general behavior of diffraction.

The diffraction efficiency in function of beam intensity for a constant intensity ratio of signal to pump 0.03 is shown in Fig. 13.

It is seen, that the diffraction efficiency does not generally grow with pump beam intensity, but the optimal intensity is observed.

Since the nonlinearity for a cross-phase modulation is positive, it is possible to observe strong exponential amplification for a pair of conjugated signal beams as a result of modulation instability process. The signal and pump wave intensities after the cell for close to optimal values of ellipticity and magnetic field are shown in Fig. 14. The output beam pattern for this process is shown in Fig. 15(b). It is seen that net amplifications of more than 100 and relative amplifications of ~1000 are easily obtained even for an unfocused beam with $r = 0.58$ mm. To avoid saturation of gain, the signal beam has to be much weaker than the pump (the ratio is ~1:10000).

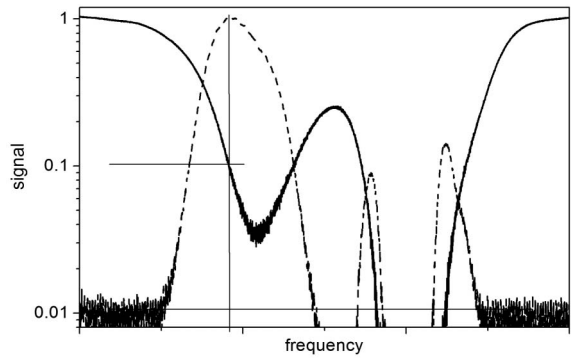

Fig. 14. Pump intensity (solid line) and signal intensity (dashed) for $P = 24$ mW, $T = 95$ °C, pump beam ellipticity 0.07, and magnetic field $B = 0.56$ G. Signals are normalized to unity at maximum.

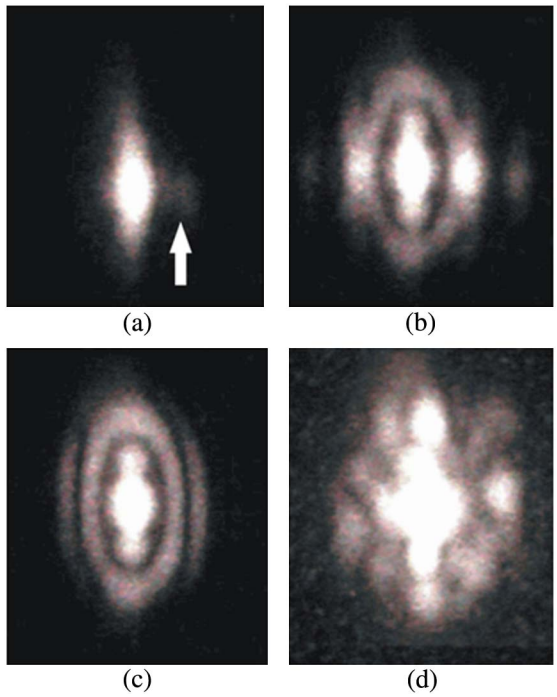

Fig. 15. (Color online) Far-field images of a beam shape after a cylindrical lens for elliptic pump polarization obtained with 7°. rotation of quarter wave plate. Temperature 98 °C (a) $F_g = 1$ line, zero magnetic field, the signal wave position is marked by an arrow. (b) Modulation instability amplifies the signal and conjugate order, $F_g = 1$ line center, beam power 2.5 mW, magnetic field 1.2 G. (c) Pump beam shape modification for the conditions of image *b*. (d) For $F_g = 2$ transition the pump is further broken into a number of spots: beam power 27 mW, magnetic field 1.8 G. The vertical size of images corresponds to 20 mrad.

For high gains the absorption is quite big (Fig. 14), and to obtain bigger self-action effects, the beam shape has to be manipulated. The intensity diminishes along the path due to the absorption, and this can be at least partly compensated by making the beam narrower along propagation. The simplest way of doing this is by means of a cylindrical lens. By adjusting polarization state and magnetic field, strong self-action effects can be observed in this geometry. We used a 20 cm focal length lens, which was focusing the beam approximately 5 cm after the cell. Some results are presented in Fig. 15. The breakup pattern appears for polarization and magnetic field parameters close to observable modulation instability range. The particular breakup pattern is highly sensitive to beam shape and to the parameters which affect the nonlinearity strength. In particular, symmetry loss is observed to a smaller or bigger extent.

5. CONCLUSION AND DISCUSSION

In conclusion, the numerical solution of the full density matrix evolution equation permits good estimation of factors affecting vectorial nonlinearity strength in rubidium vapor, and it provides useful guidelines for experiments. It follows that for obtaining strong nonlinear effects at moderate intensities it is necessary to adjust polarization state, light intensity, magnetic field and beam geometry—all of these factors contribute significantly. Simply increasing the light intensity can be counterproductive and cause the decreased nonlinearities. Strong self-action can be obtained with vectorial mechanism

in beams, which are not tightly focused. The resulting nonlinearity is unusually complicated and nonlocal.

One of our purposes here was to demonstrate strong self-action in beams. We concentrated on $F_g = 2$ line, because working with this line produces larger effects with tunable semiconductor laser. In $F_g = 1$ transition, the effects which are significant, but smaller can be obtained with one order of magnitude lower laser power.

The nonlinearity enhancement resulting from vectorial mechanism can be demonstrated for a three-level lambda configuration, for which the calculation can be done analytically. This approximation is discussed in [22]. We do not reproduce this analysis here because the three-level configuration in a steady state is clearly insufficient to describe in detail the observed behaviour. The advantage of the reported numerical modelling is a possibility to compare the theoretical description directly with an experiment without fitting parameters. The numerical approach, however, does not identify relatively simple level configurations which are directly responsible for the effect. Such identification can be important for better qualitative understanding of the mechanism.

In the investigated cases (see Figs. 4 and 8) the main part the nonlinearity enhancement is due to the cross-phase modulation, without the magnetic field. Introducing elliptic polarization and magnetic field can result in relatively smaller addition. However, this small addition can produce very significant effects when the balance between absorption and exponential amplification is important, for example, in pattern generation [1]. The enhancement due to the magnetic field is seen in the experiment, as well as in the numerical modelling, but which is a minimal level configuration leading to it, is not clear for a moment.

ACKNOWLEDGMENT

The work is done within the CONACyT project CB/156891.

REFERENCES

1. P. Zerom and R. W. Boyd, "Self-focusing, conical emission, and other self-action effects in atomic vapors," in *Self-focusing: Past and Present*, Vol. 114 of Topics in Applied Physics, R. W. Boyd, S. G. Lukishova, and Y. R. Shen, eds., (Springer Science+Business Media, 2009), pp. 231–251.
2. B. E. A. Saleh and M. C. Teich, *Fundamentals of Photonics* (Wiley, 1991).
3. M. Fleischhauer, A. Imamoglu, and J. P. Marangos, "Electromagnetically induced transparency: optics in coherent media," Rev. Mod. Phys. **77**, 633–673 (2005).
4. E. Arimondo, "Coherent population trapping in laser spectroscopy," in *Progress in Optics*, E. Wolf, ed. (Elsevier Science, 1996), Vol. 35, pp. 257–354.
5. D. Budker, W. Gawlik, D. F. Kimball, S. M. Rochester, V. V. Yashchuk, and A. Weis, "Resonant nonlinear magneto-optical effects in atoms," Rev. Mod. Phys. **74**, 1153–1201 (2002).
6. A. M. C. Dawes, L. Illing, S. M. Clark, and D. J. Gauthier, "All-optical switching in rubidium Vapor," Science **308**, 672–674 (2005).
7. E. E. Mikhailov, A. Lezama, T. W. Noel, and I. Novikova, "Vacuum squeezing via polarization self-rotation and excess noise in hot Rb vapors," J. Mod. Opt. **56**, 1985–1992 (2009).
8. I. H. Agha, G. Messin, and P. Grangier, "Generation of pulsed and continuos-wave squeezed light with (87)Rb vapor," Opt. Express **18**, 4198–4205 (2010).
9. C. Liu, J. Jing, Z. Zhou, R. C. Pooser, F. Hudelist, L. Zhou, and W. Zhang, "Realization of low frequency and controllable bandwidth squeezing based on a four-wave-mixing amplifier in rubidium vapor," Opt. Lett. **36**, 2979–2981 (2011).
10. N. Ram, M. Pattabiraman, and C. Vijayan, "Low field Zeeman magnetometry using rubidium absorption spectroscopy," J. Phys. Conf. Ser. **80**, 012035 (2007).
11. R. Zhang, J. A. Greenberg, M. C. Fischer, and D. J. Gauthier, "Controllable ultrabroadband slow light in a warm rubidium vapor," J. Opt. Soc. Am. B **28**, 2578–2583 (2011).
12. S. R. Shin and H.-R. Noh, "Doppler spectroscopy of arbitrarily polarized light in rubidium," Opt. Commun. **284**, 1243–1246 (2011).
13. S. Mitra, M. M. Hossain, P. Poddar, C. Chaudhuri, B. Ray, and P. N. Ghosh, "Standing wave pump field induced coherent nonlinear resonances in rubidium vapor," Chem. Phys. Lett. **513**, 173–178 (2011).
14. G. Moon and H. Noh, "Analytic solutions for the saturated absorption spectra," J. Opt. Soc. Am. B **25**, 701–711 (2008).
15. N. Korneev and O. Benavides, "Mechanisms of holographic recording in rubidium vapor close to resonance," J. Opt. Soc. Am. B **25**, 1899–1906 (2008).
16. N. Korneev and O. Benavides, "Direct multi-level density matrix calculation of nonlinear optical rotation spectra in rubidium vapour," J. Mod. Opt. **56**, 1194–1198 (2009).
17. L. D. Barron, *Molecular Light Scattering and Optical Activity* (Cambridge, 2004).
18. G. S. Agarwal, *Quantum Statistical Theories of Spontaneous Emission and their Relation to Other Approaches* (Springer Verlag, 1974).
19. K. Mølmer, Y. Castin, and J. Dalibard, "Monte Carlo wavefunction method in quantum optics," J. Opt. Soc. Am. B **10**, 524–538 (1993).
20. J. Ries, B. Brezger, and A. I. Lvovsky, "Experimental vacuum squeezing in rubidium vapor via self-rotation," Phys. Rev. A **68**, 025801 (2003).
21. E. E. Mikhailov and I. Novikova, "Low-frequency vacuum squeezing via polarization self-rotation in Rb vapor," Opt. Lett. **33**, 1213–1215 (2008).
22. N. Korneev, "Nonlinearity enhancement in rubidium vapour with vectorial mechanism," Proc. SPIE **8011**, 801137 (2011).